Journal of Catalysis 408 (2022) 43–55

Contents lists available at ScienceDirect

Journal of Catalysis

journal homepage: www.elsevier.com/locate/jcat

Selective semi-hydrogenation of internal alkynes catalyzed by Pd–$CaCO_3$ clusters

Jordi Ballesteros-Soberanas [a], Juan Carlos Hernández-Garrido [b], José Pedro Cerón-Carrasco [c,*], Antonio Leyva-Pérez [a,*]

[a] Instituto de Tecnología Química (UPV–CSIC), Universidad Politècnica de València–Consejo Superior de Investigaciones Científicas, Avda. de los Naranjos s/n, 46022 Valencia, Spain
[b] Departamento de Ciencia de los Materiales e Ingeniería Metalúrgica y Química Inorgánica, Facultad de Ciencias, Universidad de Cádiz, Campus Universitario Puerto Real, 11510 Puerto Real, Cádiz, Spain
[c] Centro Universitario de la Defensa. Academia General del Aire. Universidad Politécnica de Cartagena. C/ Coronel López Peña s/n, 30720 Murcia, Spain

ARTICLE INFO

Article history:
Received 27 December 2021
Revised 22 February 2022
Accepted 23 February 2022
Available online 1 March 2022

Keywords:
Metal clusters
Minimum catalytic unit
Semi-hydrogenation of alkynes
Lindlar catalyst
Internal alkynes

ABSTRACT

The *de-novo* synthesis of soluble or solid-supported Pd-$(CaCO_3)_n$ clusters (n = 2–13) and their high catalytic activity for the semi-hydrogenation of internal alkynes compared to terminal alkynes, is presented. Mechanistic studies show that this reactivity, i.e. internal alkynes more reactive than terminal alkynes, comes from the higher electrophilicity of the Pd-$(CaCO_3)_n$ cluster compared to the nanoparticulated Lindlar catalyst, which unveils the advantages of isolating the minimum catalytic unit of a solid catalyst. Translating solid active sites into soluble catalysts turns around the classical approach and constitutes a paradigmatic shift in catalyst design.

1. Introduction

Any catalytic support, from the simpler to the more sophisticated example, is irremediably a structured extended surface with diffusion limitations, potential energy wells and undesired adsorption sites, and these drawbacks are not generally addressed but simply assumed [1]. When metals are involved, the design of the catalyst is mainly devoted to increase the efficiency of the metal active site, which is often achieved with ligands for soluble catalysts and with structured and high surface area frameworks for solid catalysts [2–5]. Fig. 1A shows the approach presented here, which consists in synthesizing, independently, the catalytically active molecular entity of a metal-supported solid. This strategy allows the reproduction of the catalytic activity of the whole solid catalyst without the need of the whole extended structure and, thus, without the above commented limitations for bulk solids. In this way, the new soluble cluster catalyst is ready to be used either in solution or re-supported onto a new solid. This short molecule can be viewed as the "minimum catalytic unit" of the solid, a concept only recently explored by Pérez-Ramirez and collaborators in heterogeneous catalysis [6,7] despite the analogous concept being historically well studied in enzymes [8–11].

The Lindlar catalyst (Pd–Pb nanoparticles supported on calcium carbonate) is the catalyst of choice for the semi-hydrogenation of alkynes to cis-alkenes [12,13]. The extensive use of the Lindlar catalyst in fine chemistry, pharma and natural product synthesis is not surprising considering that the alkene group is the most prevalent functionality in these organic compounds [14,15]. It is accepted that Pd atoms activate the alkyne and dissociate H_2 while the surrounding $CaCO_3$ tunes the Pd electronics and co-adsorbs the slightly acid terminal alkyne [16]. Pb acts as an alloying agent to avoid excessive Pd agglomeration [17] and subsequent sub-surface hydride formation [18–21], and the extended $CaCO_3$ surface does not provide apparent benefits in terms of substrate diffusion, although in some cases it has been reported to palliate substrate polymerization [22]. It is widely accepted that the Lindlar catalyst selectivity towards the alkene formation stems from a control of the substrate adsorption on the Pd active site. More specifically, the alloyed Pb tunes the adsorption energies of the adsorbates on the Pd active site, making the adsorption of the alkene unfavorable while maintaining a fairly exothermic alkyne adsorption [12]. Nonetheless, commercially-available colloidal Pd nanoparticles free of Pb [23] (c-Pd/TiS, see below) have shown an excellent catalytic activity for the cis-selective

* Corresponding authors.
E-mail addresses: jose.ceron@cud.upct.es (J.P. Cerón-Carrasco), anleyva@itq.upv.es (A. Leyva-Pérez).

https://doi.org/10.1016/j.jcat.2022.02.020
0021-9517/

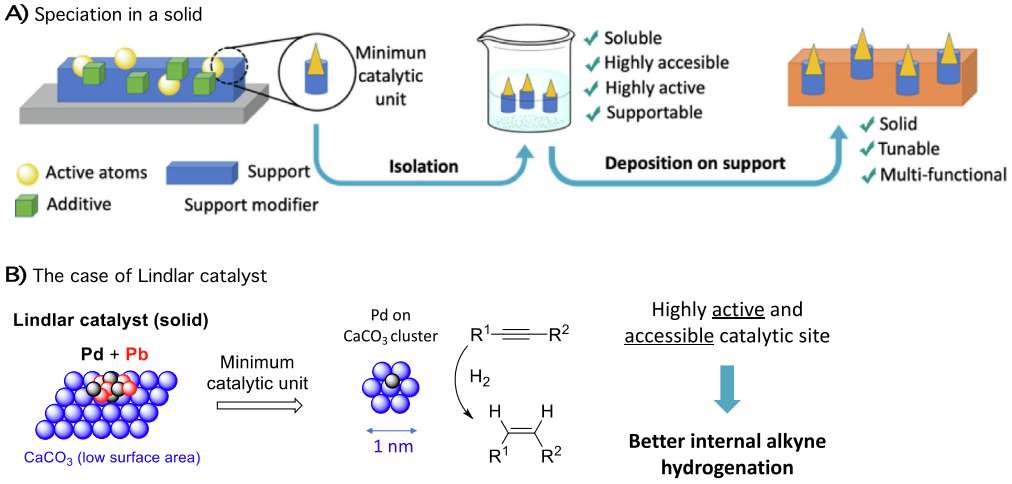

Fig. 1. Lindlar catalyst as a proof of concept for the speciation of minimum catalytic units in a solid. A) Catalyst design by speciation (de-novo synthesis) of the minimum catalytic unit of a solid, and its later use in solution or re-supported. B) Scheme of the Lindlar catalyst structure and the potential minimum catalytic unit.

semi-hydrogenation of alkynes, which support that the removal of Pb does not have to be detrimental for the Pd action [24]. Other less toxic metals have been employed as alloying agents to successfully imitate the role of Pb in the Lindlar catalyst [25,26], or as decorating agents, alongside lighter elements like B, S or P, to achieve more beneficial electronic properties on Pd [7,27,28].

Terminal alkynes have traditionally shown higher reactivity than internal alkynes during the semi-hydrogenation reaction, which can be explained by a better steric accommodation of the former onto the Pd site, taking also in account the concomitant H_2 adsorption [29–32]. Indeed, acetylene is often regarded as the most reactive alkyne in this reaction [16,33]. However, in electronic terms, internal alkynes are better π-electron donors than terminal alkynes and, consequently, could easily coordinate cationic Pd sites and suffer the semi-hydrogenation reaction provided that the catalytic site is sterically available [34,35].

Fig. 1B shows our hypothesis here, which envisions that the minimum catalytic unit of the Lindlar catalyst is a single or few Pd atoms with its surrounding calcium carbonate [$(CaCO_3)_n$]. If such a sub-nanometric chemical entity could be prepared [36,37], all the (toxic) additives of the solid catalyst will be avoided, and the catalytic site will be more available for hindered internal alkynes [38,39]. In principle, this Pd-$(CaCO_3)_n$ catalyst can be either in solution or supported on solids, at wish. We show here the synthesis of such Pd-$(CaCO_3)_n$ catalysts and their high catalytic activity for the hydrogenation of internal vs. terminal alkynes.

2. Materials and methods

Materials. Chemicals **1**–**6** and **12**–**30** were purchased from Millipore-Sigma (96–99% purity). Chemicals **7**–**11** were purchased from TCI Chemicals (97–98% purity) and 5-decyn-1-ol, used for the synthesis of 5-decynylacetate, was purchased from Abcr (97% purity). They were purchased and used as received. $Pd_2(dba)_3$ was purchased from Millipore-Sigma (97% purity).

Physical Techniques. The metal content of the samples was determined by inductively coupled plasma-atomic emission spectroscopy (ICP-AES). Solids were disaggregated in aqua regia and later diluted before analysis. FT-IR spectra were recorded on a spectrophotometer as KBr pellets. Attenuated total reflection infrared spectroscopy was used to obtain the spectra of the Pd-$(CaCO_3)_n$ clusters, from 400 to 4000 cm^{-1} by dropping a small sample of the clusters in the liquid and solid phase on the ATR crystal. The fragmentation pattern of the carbonate chains was obtained with a UPLC-MS instrument, by directly infusing the liquid sample into the electrospray ionization chamber. The mass spectrometry was performed with a time-of-flight detector. XPS measurements were performed on a SPECS spectrometer equipped with a Phoibos 150 MCD-9 analyser using a non-monochromatic Mg KR (1,253.6 eV) X-ray source working at 50 W. The C1s peak has been set at 284.5 eV as the internal reference for the peak positions in the XPS spectra. X-Ray diffraction spectra of the support and supported catalyst were recorded in a CubiX PRO (PAN Analytical) spectrometer, with a Cu K(α) radiation source, 1.5406 Å wavelength. GC and GC-MS chromatography were performed in chromatographs with 25 m capillary columns filled with 1 or 5 wt% phenylsilicone. ^1H, ^{13}C and DEPT NMR spectra were recorded at room temperature on a 300.1 MHz spectrometer. Absorption spectra were recorded on an UV/Vis spectrophotometer in 1 cm wide cuvettes.

Advanced electron microscopy characterization. Aberration Corrected High Resolution (Scanning) Transmission Electron Microscopy (AC-HR-(S)TEM) was employed to image the Pd-$(CaCO_3)_n$ clusters, performed on a FEI Titan Thermis 60–300 Double aberration corrected, operated at 200 kV, with 21.4 mrad beam convergence angle, using 115 mm camera length and 48–200 mrad collection angle range. The images of the c-Pd/TiS catalyst and the commercial Pd on C (1%) were obtained on a JEM-F2100 operated at 200 kV in Dark Field scanning transmission electron microscopy (DF-STEM mode). High Resolution Field Emission Scanning Electron Microscopy (HR-FESEM). The images of the Lindlar catalyst were obtained in a ZEISS Ultra 55 SEM, operated at 1.5 kV using the backscattered electron in-lens detector (ESB).

Computational methods. As noted in the main text, two strategies are implemented to yield to reliable structures. The first approach uses the isolated components of the cluster, which is the only input data required for performing calculations with the recently developed crystal structure analysis by particle swarm optimization (CALYPSO) code [40,41]. In short, CALYPSO is based on a particle swarm optimization algorithm that is fed with the number of every element, that is, atoms are randomly combined to generate all possible combinations without imposing any initial bond order [42]. In the second method, we considered the predicted lowest energy configurations reported by Chen, Dixon and co-workers for a series of $(CaCO_3)_n$ nanoclusters [43]. These authors performed genetic algorithm-based simulations to assess the structural trend during $CaCO_3$ aggregation phenomena. The deposited $(CaCO_3)_3$ structure is re-optimized here by

simultaneously exploring the surface with a Pd metallic center. All generated structures are next relaxed within a dispersion-corrected density functional theory (DFT-D) framework as implemented in Gaussian16 [44]. These calculations are performed by coupling the ωB97X-D functional developed by Chai and Head-Gordon [45] to the Def2SVP basis set for all atoms except Pd, where the latter center is treated with the corresponding relative effective core potential (Def2-ECP) version [46,47]. To ensure the stability of the optimized cluster (i.e. minima in the potential energy surfaces), a vibrational analysis is systematically conducted to confirm the absence of normal modes with imaginary frequencies. Solvent effects are accounted for with the polarizable continuum model (PCM) using the parameters for ethanol [48].

To the mimic semi-hydrogenation reactions, Alkynes **1** and **4** are selected as representative species with large and small TOFs values, respectively. To be consistent with earlier steps, the systems are then fully optimized at the ωB97X-D/Def2SVP-ECP level of theory, and the interaction energy computed by using the total energy of the separated reactants as a reference value. The reduced density gradient is used for resolving non-covalent interactions energies with NCI-Plot code as implemented in Jaguar [49–52]. The nature of transition states (TSs) is confirmed by one single imaginary frequency that correspond to the reaction coordinate. Additional scans at 0.1 angstroms step along with the reactions coordinate and IRC calculations are performed to confirm that TSs correctly connect reactants and products.

Synthetic procedures. Preparation of Pd-$(CaCO_3)_n$ clusters. A volume of 100 mL of ethanol was saturated with 0.2–1 mg of $Pd_2(dba)_3$, although the purity and ageing of the commercial precursor conditioned the amount required. This is a well-known issue with this precursor, and has been published in the past [53]. Up to 10 mg of precursor were used in some batches, due to most of it having degraded to Pd black. To bypass this issue, the mixture was stirred for 15 min to dissolve as much precursor as possible. Then, the solution was centrifugated and further filtrated (400 nm filter) to eliminate impurities from the precursor, redoing the process until the desired concentration was obtained (0.5–2 ppm Pd in solution, as $Pd_2(dba)_3$). The obtained solution should be violet-colored and completely transparent. 200 mg of $CaCl_2{\cdot}2H_2O$ were added to the solution and sonicated to disperse the salt. After having fully dissolved, the solution was placed into a 250 mL round flask with stirring (300 rpm) where 1.2 mL of TEA were added. After the addition of the amine, CO_2 started to flow from a reservoir to the flask through a capillary at 100 cm^3/min during 5–10 min. The violet color of the solution starts to fade after sonicating and adding the base, and becomes almost colorless when the CO_2 bubbling starts. Upon bubbling, the solution becomes turbid, indicative of the $CaCO_3$ being formed, and becomes transparent again due to the amine, which is capping the carbonate chains and making them stable in the liquid phase. After the bubbling stops, the solution is kept in stirring for 10–30 more minutes. The stirring times after the exposure to CO_2 were dependent on the amount of time the solution required to shift back from white to transparent, which varied depending on the specific synthesis. The obtained solution is centrifuged at high speed (20,000 g), washed and rinsed 3 times with fresh ethanol. Higher metal loadings and longer bubbling times lead to the formation of bigger Pd aggregates, while lower loadings and shorter bubbling times lead to the formation of more disperse, smaller Pd clusters.

Synthesis of 5-decynylacetate. 100 mg of 5-decyn-1-ol (0.65 mmol) was dissolved in 15 mL of anhydrous CH_2Cl_2 and cooled under N_2 to 0 °C. 78.5 mg (1 mmol) of acetyl chloride were dissolved in 50 mL of anhydrous CH_2Cl_2 under N_2, and added dropwise to the 5-decyn-1-ol solution. The reaction was kept in stirring for 2 h, and quenched afterwards in 15 mL of cold water. The mixture was extracted with CH_2Cl_2, dried over $MgSO_4$ and purified by column chromatography.

Semi-hydrogenation reactions. All the batch reactions in this work were performed in a 6-mL round bottom vial with a stirring magnet, in 0.5 mL of ethanol, and 0.3 mmol of starting material, otherwise stated. The reactions were conducted at room temperature and stirred at 450 rpm, in a H_2 pressurized atmosphere of 3 bars. The H_2 pressure was kept constant by refilling the reactor periodically. At the start of the reaction, the alkyne: H_2 molar ratio was roughly 1–2.5, and enough H_2 was always present to fully hydrogenate the alkyne to the corresponding alkane. The yields were obtained by gas chromatography, and gas chromatography-mass spectrometry and NMR were used to identify the products.

3. Results and discussion

3.1. Synthesis and characterization of Pd-$(CaCO_3)_n$

Pd-$(CaCO_3)_n$ was successfully formed by saturating with CO_2 an ethanol solution containing triethylamine (TEA), $CaCl_2$ and $Pd_2(dba)_3$. Pd^{II} precursors were rapidly reduced under these synthesis conditions and led to the formation of Pd nanoparticles, in contrast to $Pd_2(dba)_3$. Triethylamine has a double role, acting as a capping agent to prevent further growth of the calcium carbonate oligomers and displacing the dibenzilideneacetone (dba) ligands from the Pd precursor, as observed by UV-Vis experiments (Figure S1 and Table S1). The final ethanolic solution contains 0.90–1.40 ppm of Pd and 400–600 ppm of Ca, measured by inductive coupled plasma-atomic emission spectroscopy (ICP-AES). Fig. 2a shows the attenuated total reflection infrared spectrum (ATR-IR) of the Pd-$(CaCO_3)_n$ solution, which reveals a shoulder at 860 cm^{-1} corresponding to the C–O band of carbonate [54], as well as a band at 1640 cm^{-1} attributed to the N··H hydrogen bond. The latter can also be assigned to the protonated carbonate group capped by triethylamine [55]. Fig. 2b shows the high pressure liquid chromatography-mass spectrum (HPLC-MS) of the solution, where the presence of carbonate chains of different lengths, ranging from 2 to at least 13 units can be observed.

The Pd-$(CaCO_3)_n$ solution was impregnated on γ-alumina, in order to obtain a heterogeneous, easier to handle catalyst, while simultaneously enabling the re-concentration of the Pd species in the liquid phase onto the alumina surface [55]. Fig. 2c shows aberration corrected high-resolution-high angle annular dark field-scanning transmission electron microscopy (AC-HR-HAADF-STEM) images of the supported Pd-$(CaCO_3)_n$ species on γ-alumina, where a distribution of Pd species. On 2c, left, a general overview of the catalyst: Pd species present solely on $CaCO_3$, supported on Al_2O_3. On 2c, center, a close-up of some small, structured Pd NPs next to less-ordered, sub-nanometrical clusters and single atoms is presented. Some lattice fringes from the structured, underlaying oxide can be observed on the left edge of the image. At maximum resolution (2c, right) some single atoms can be observed on the amorphous $CaCO_3$. It is worth mentioning that the sizes of the Pd species in this catalyst are lower than the usual size of nanoparticles prepared in solution, which ranges from 4 to 10 nm [56–59], likely due to the very low Pd contents in the solution. However, it must be emphasized here that the 1–2 nm Pd nanoparticles are possible not the catalytic active species but <1 nm Pd species (see ahead). The Pd species can be found on the $CaCO_3$ islands formed on top of the alumina support. The presence of the carbonate species on the solid was further confirmed by Fourier-transformed infrared spectroscopy (FT-IR, Figure S2). Representative bands of crystalline $CaCO_3$ were not observed on the X-Ray diffraction (XRD) spectra of the Pd-$CaCO_3$/Al_2O_3 powder, which indicates the formation of very tiny and

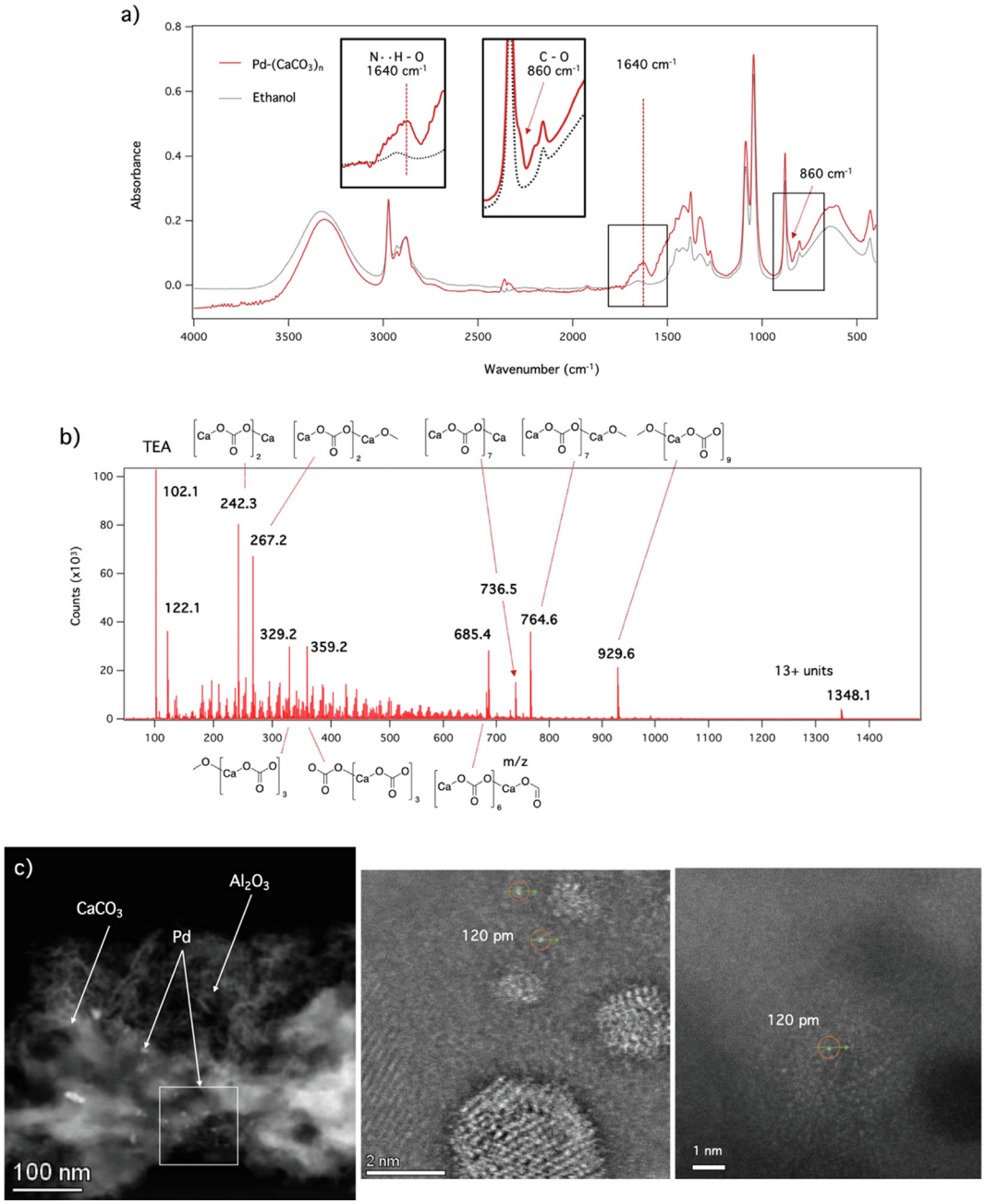

Fig. 2. ATR-IR (a) and TOF-MS (b) spectra of the ethanolic Pd-$(CaCO_3)_n$ solution, and AC-HR-HAADF-STEM imaging of Pd-$(CaCO_3)_n$ on Al_2O_3 (c). The lattice fringes on the left of the middle picture correspond to the structured oxide support underneath the amorphous $CaCO_3$.

amorphous carbonate phase. Similarly, peaks corresponding to a crystalline Pd phase were not observed on the supported catalyst, as expected for Pd species of less than 2 nm (Figure S3). XPS analysis was also performed on the supported catalyst, and confirmed the presence of Ca on the sample, with the characteristic $CaCO_3$ $2p_{3/2}$ - $2p_{1/2}$ splitting, by roughly 3.5 eV. A faint band at 342.1–341.9 eV was observed and assigned to the Pd $3d_{3/2}$ orbital; a higher binding energy than the characteristic bulk Pd signal (340.7 eV), a shift usually observed for very small Pd clusters [60] or in Pd-O environments [61,62], which could originate in this case from the interaction of Pd and the underlaying $CaCO_3$. (Figure S4) The Pd $3d_{5/2}$ band, expected at ~ 336 eV, could not be determined. The presence of sub-nanometric clusters in the Pd-$(CaCO_3)_n$ catalysts contrasts with the other two commercial catalysts, the c-Pd/TiS catalyst and the Lindlar catalyst. Nanoparticles with a narrow size distribution were observed on the c-Pd/TiS catalyst (Figure S5), in accordance with previous results [23], and Pb-alloyed Pd species of greatly disparate sizes were observed by high-resolution field emission-scanning electron microscopy (HR-FESEM) on the Lindlar catalyst (Figure S6), ranging from 10 nm to 500 nm. For the sake of comparison, images of commercial Pd on carbon (1 wt% Pd) were also obtained (Figure S7).

Given the extraordinarily low concentration of Pd in the catalyst, either supported or not, other routinely characterization techniques could not be performed. Thus, discerning if Pd single atoms [63–66] or few atoms clusters [63,64,67–69] are the major species in Pd-$(CaCO_3)_n$ is difficult at this point. However, the data collected in this section together with mechanistic and computational studies (see below) will give a reasonably accurate picture of the catalyst structure.

3.2. Catalytic results

Fig. 3 shows the catalytic activity of soluble Pd-$(CaCO_3)_n$ compared to the commercial Lindlar and c-Pd/TiS catalysts, for the partial hydrogenation of different alkynes to the corresponding cis-alkenes. The catalytic activity was evaluated in a batch reactor at room temperature, under pressurized H_2 atmosphere (3 bar) and constant stirring. The initial semi-hydrogenation turnover frequency (TOF_0, calculated from a linear regression of the initial kinetic points, typically up to 30% conversion) of Pd-$(CaCO_3)_n$ for the internal *gemini* alkyne 2,5-dimethyl-3-hexyn-2,5-diol **1** and 4-octyne **2** is 10 times higher than the commercial Lindlar and c-Pd/TiS catalysts, and double for 3-methyl-1-pentyn-3-ol **3** and diphenylacetylene **4**, although lower for phenylacetylene **5**. The hydrogenation of **3** did not proceed without the addition of the Pd precursor to the $CaCO_3$ solution and another blank test with $Pd_2(dba)_3$ in ethanol proceeded at a much slower rate, with a TOF_0 45 times lower than with Pd-$(CaCO_3)_n$ (Figure S8). The activity of two different catalyst batches fell within the same range, proving the reproducibility of the catalyst synthesis.

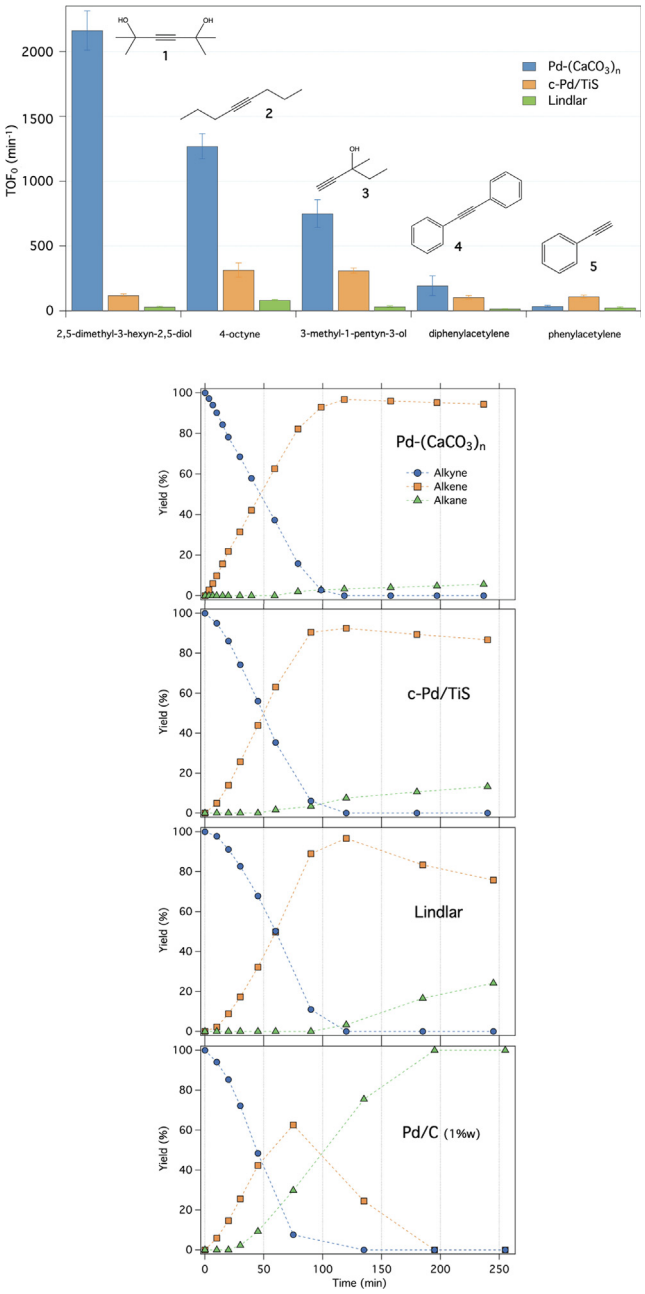

Fig. 3. Top: Alkene formation initial turnover frequencies (TOF_0) of the screened catalysts for different alkynes. Bottom: Kinetic profiles for the hydrogenation of **3** with a) Pd-$(CaCO_3)_n$ (1.2 ppm Pd), b) c-Pd/TiS catalyst (2.3 ppm Pd), c) the Lindlar catalyst (7.0 ppm Pd), d) Pd NPs on carbon (4.1 ppm Pd). Reactions were carried out at 298 K under 3 bars of H_2.

Further examination of the catalytic results in Fig. 3 show that the reactive differences between Pd-$(CaCO_3)_n$ and the commercial catalysts arise not only from the overall catalytic activity but also from a much better semi-hydrogenation of internal vs terminal alkynes, with Pd-$(CaCO_3)_n$, which contrasts with the often mixed results found in bibliography for the commercial Pd catalysts (Table S2). The lower activity for internal alkynes of the commercial catalysts is particularly visible for c-Pd/TiS, in accordance with its reported inefficiency when hydrogenating alkynes with a kinetic radius superior to 8 Å [12], due to the steric impediments imposed by the hexadecyl-(2-hydroxyethyl)dimethyl ammonium dihydrogen-phosphate (HHDMA) ligand tails (Table S2). Besides, regardless of the position of the alkyne in the aliphatic substrate, the Pd-$(CaCO_3)_n$ catalyst shows a much more pronounced selectivity towards the alkene during extended reaction times, as evidenced by the kinetics results in Fig. 3. The different kinetic experiments were carried out at a similar reaction rate, for a fair comparison of the selectivity vs time for all Pd catalysts, thus using the different amounts of Pd specified in Fig. 3. It can be seen there that Pd-$(CaCO_3)_n$ selectively catalyzes the semi-hydrogenation of **3** to 3-methyl-1-penten-3-ol (**3′**) with a yield of 96.7% after 100 min, and this selectivity is maintained for at least two more hours. Only a 3.3% of the corresponding alkane is formed after full conversion. In contrast, the colloidal Pd catalyst presented a lower selectivity after full conversion, with a maximum percentage of alkene of 92.5%, and the Lindlar catalyst reached the same yields but rapidly overhydrogenated the product when there was no remaining alkynol [70], which is a well reported issue for this catalyst. The Pd/C catalyst, as expected, showed very low selectivity. Similar results were found for alkynes **1** and **2** (Figure S9). These results suggest an excellent selectivity control of the soluble Pd-$(CaCO_3)_n$ catalyst together with a much superior performance respect to the commercial catalysts.

As a means to further investigate the aforementioned trends in activity and to extent the potential use of the Pd-$(CaCO_3)_n$ catalyst, we performed a scope of aliphatic and aromatic alkynes, both terminal and internal. Fig. 4 shows that internal aliphatic alkynes are the fastest reacting substrates on the Pd-$(CaCO_3)_n$ catalyst. Compounds **1**, **2** and **15**–**23** hydrogenate selectively to the corresponding cis-alkene products with full or nearly full conversion in all cases. The presence of an oxygen-atom containing propargyl substituent (hydroxyl, ketone or ester) positively affects the reaction rates (Figure S10), and only internal aromatic alkynes lacking this substituent are less reactive (compounds **4** and **12**–**14**, with exception of alkyne **21**). It is worth mentioning that no aldehyde to alcohol conversion was observed for substrates **6** and **24**, that the halogenated rings in substrates **9** and **10** were also tolerated, and the main reaction of **12** and **23** was the hydrogenation of the internal alkyne groups to give the corresponding dienes as main products. Pd-$(CaCO_3)_n$ supported on γ-Al_2O_3 was also active and highly selective for the semi- hydrogenation of substrates **2**, **3**, **18** and **20**, which gave the corresponding alkenes in comparable yields to the homogeneous catalyst. A "hot filtration" test was performed with the supported catalyst and neither leaching evidence (Figure S11) nor particle aggregation were detected (Figure S3). However, the catalyst could not be directly reused after reaction with **3**, which indicates that a reactivation process might be necessary to regenerate the catalyst.

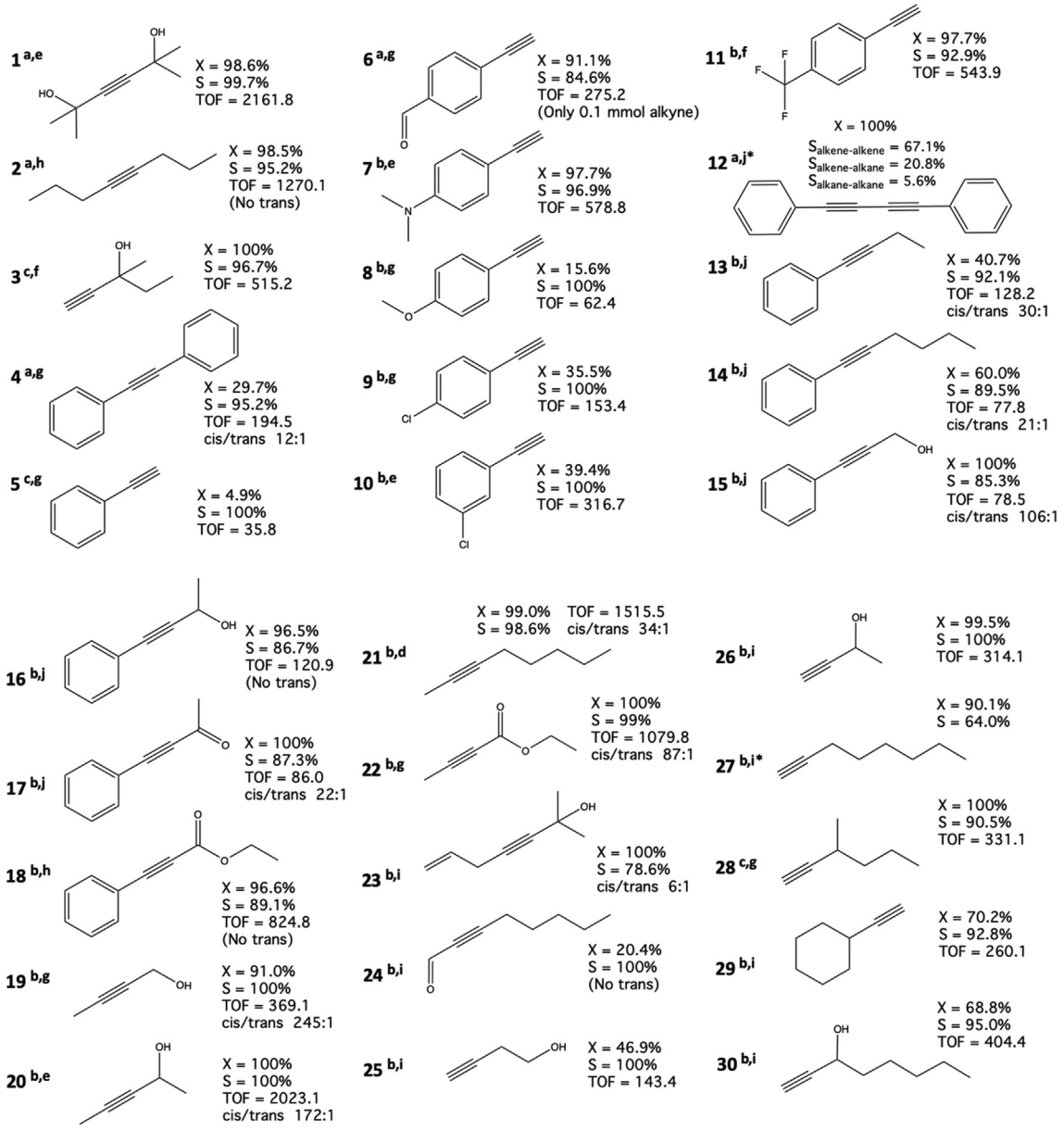

Fig. 4. Scope for the semi-hydrogenation of different alkynes with the Pd-$(CaCO_3)_n$ catalyst; X = conversion of the alkyne (starting material), S = selectivity towards alkene, otherwise specified, TOF (min^{-1}) of the alkyne to alkene reaction. The conditions under which the reactions were performed can be found next to the substrate number, which are the following: a) 0.46 ppm Pd, b) 1.20 ppm Pd, c) 1.40 ppm Pd; d) 60 min, e) 90 min, f) 120 min, g) 150 min, h) 180 min, i) 240 min, j) 12 h of reaction time, k) Pd-$(CaCO_3)_n$ on alumina catalyst. All reactions were performed at room temperature, except for some performed at 333 K (*), which did not proceed at room temperature. All reactions were performed with 0.3 mmol of alkyne as a starting material, otherwise specified.

3.3. Reaction mechanism

3.3.1. Nature of the active Pd sites

In order to assess the nature of the catalytically active Pd species in the Pd-$(CaCO_3)_n$ clusters, poisoning tests were performed with triphenylphosphine (PPh_3), which has been reported to easily bind to the metal site and displace ligands such as dba [71]. The supported Pd-$(CaCO_3)$n on γ-alumina was employed for a fair comparison with the commercial supported catalysts in terms of PPh_3 adsorption. Fig. 5a shows that, when poisoned with a 1:20 Pd-$(CaCO_3)_n$ to PPh_3 ratio, the γ-alumina-supported Pd-$(CaCO_3)_n$ catalyzed hydrogenation of **3** is almost stagnant, with a 96% less alkene being formed. In striking contrast, Fig. 5b-c show that the c-Pd/TiS and Lindlar catalysts were just partially poisoned by PPh_3, with final alkene yields > 90%. It is worth noting that the poisoning agent generated an induction period for both the Lindlar and the c-Pd/TiS catalysts, responsible for the low yields at 1 h reaction time, which is not the case for the Pd-$(CaCO_3)_n$ on alumina, where the semi-hydrogenation reaction did not start after 8 h. The ability of the Lindlar catalyst to selectively hydrogenate alkynes stems from the favorable adsorption of the alkyne group compared to the alkene group [12], although selective and unselective sites have been identified on the catalyst surface [70]. In accordance, as shown above in Fig. 3c, high yields of **3′** are only achieved while some alkyne **3** remains in solution. Otherwise, quinoline poisoning is needed to palliate the alkene over-hydrogenation [72] at expenses of a further activity loss, in addition to the losses caused by lead-poisoning [73]. c-Pd/TiS operates similarly to the Lindlar catalyst in terms of adsorption energies, but the destabilization of the adsorbates is promoted by the organic ligand (HHDMA)

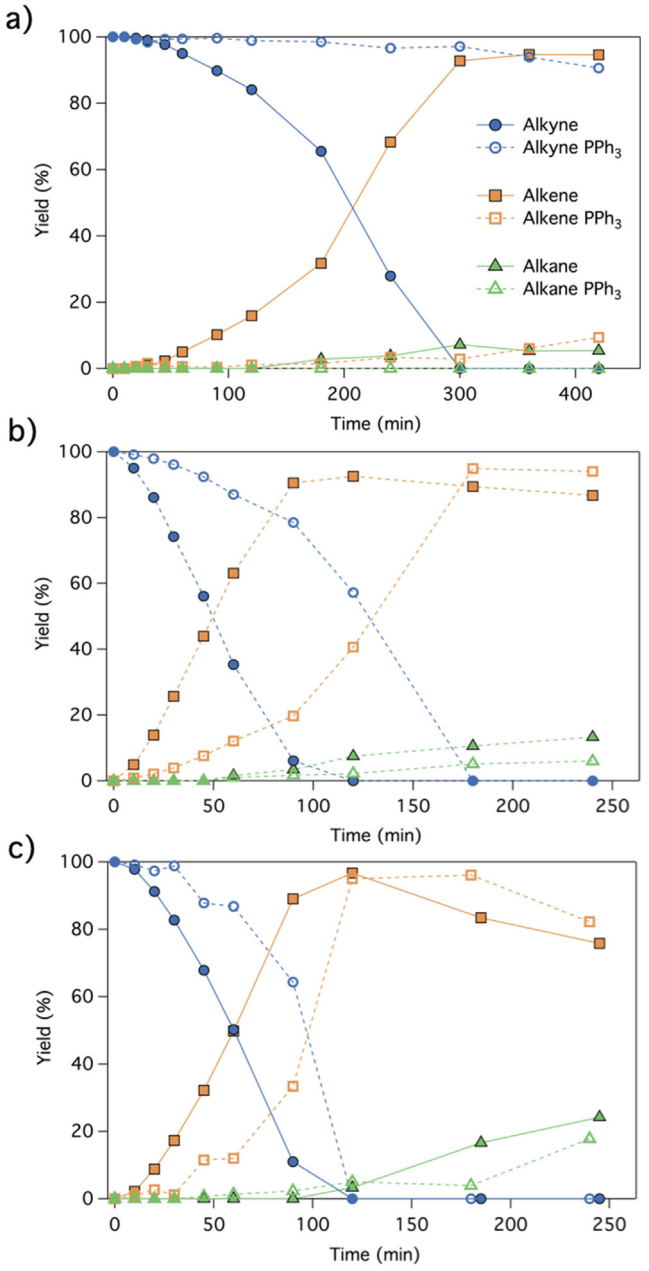

Fig. 5. Kinetic profiles for the hydrogenation of **3** untreated (full markers), and treated with PPh_3, Pd:PPh_3 ratio 1:20 (empty markers): a) Pd-$CaCO_3$ on γ-Al_2O_3, b) c-Pd/TiS, c) Lindlar catalyst.

monolayer that is present on the nanoparticle surface [12]. Besides, the steric effects caused by the presence of the phosphate organic monolayer decreases the accessibility of the alkyne to the catalytic site, a phenomenon observed on other functionalized catalysts with phosphonic ligands [74].

3.3.2. Alkyne effect

The Pd-$(CaCO_3)_n$ catalyst outperforms the two commercial catalysts in terms of intrinsic activity and selectivity. Therefore, the key to its selective hydrogenation performance might be attributed not only to the size of the Pd species but also to their intrinsic electronic properties. The high selectivity of Pd single atoms for the partial hydrogenation of acetylene has been attributed to lower ethylene adsorption energies [75] and a higher electron density of the Pd single atom, which would favor a charge transfer into the unoccupied π orbital of acetylene, which would in turn destabilize the triple bond [76]. Thus, in view of these results and our experimental data pointing towards the importance of electronic effects [7,77,78], reaction rates for differently substituted aromatic alkynes were correlated with the Pd-$(CaCO_3)_n$ catalyst through the Hammett equation. In contrast to the reported absence of correlation between hydrogenation rates and alkyne charge for the Lindlar catalyst [79], Fig. 6 shows that the Pd-$(CaCO_3)_n$ catalyst presents a *v-shaped* Hammett plot [80,81], suggesting a change in the mechanism ruled by the induced charge in the alkyne group. This catalyst performs well in the presence of both electronically dense and charge deficient alkynes, with the least reactive substrate being phenylacetylene (σ = 0). The slope values obtained for Pd-$(CaCO_3)_n$ (ρ_{EDG} = -3.20, ρ_{EWG} = +5.38) emphasize the strong dependence of the reaction rates on the charge of the alkyne, as well as a partial poisoning of the catalyst in the presence of phenylacetylene, alluded to by the high slope observed in the EWG regime. In fact, when the formation of larger nanoparticles is induced on the Pd-$(CaCO_3)_n$ catalyst, phenylacetylene does not poison the catalyst and the reaction proceeds (Figure S12). From our computational results (*vide infra*), we infer that the formation of styrene could be highly impeded on the limited Pd surface of Pd-$(CaCO_3)_n$ due to the binding mode of the substrate, while it could proceed normally on the extended Pd surface of a nanoparticle.

The high dependence of the reaction rates on the charge of the alkyne, illustrated by the slopes of the Hammett plot, and the potential poisoning effects of phenolic substrates, explains the observed enhanced performances of internal aliphatic alkynes, which generally possess more inductive substituents, and make case for the wide array of different TOFs presented in Fig. 4 [82].

3.3.3. H_2 effect

Fig. 7a shows that the hydrogenation rates of 1-ethynyl-4-dimethylaniline (**7**) and 4-trifluoromethylphenylacetylene (**11**) have a slight negative dependence on the alkyne concentration, with reaction orders of −0.19 ± 0.01 and −0.06 ± 0.01, while in contrast, the reaction rates show a strong dependence on the hydrogen pressure, with reaction orders of 0.82 ± 0.13 and 1.00 ± 0.05, respectively (Figure S13). These dependences can be linked to the Langmuir-Hinshelwood/Hougen-Watson (LHHW) models involving the adsorption of two reagents. Comparing the curves in Fig. 7 with the theoretical curves for the most probable LHHW models [83], it becomes apparent that the best fitting model involves a single catalytic site, in which the alkyne and H_2 adsorb competitively, while H_2 controls the reaction rate (Figure S14).

Primary kinetic isotope effects (KIEs) were observed when performing the semi-hydrogenations of **7** and **11** with D_2. Switching hydrogen for deuterium approximately halved the reaction rates of **7** and **11**, with KIE values of k_H/k_D = 2.1 ± 0.1 and k_H/k_D = 2.3 ± 0.2, respectively (Figure S15). The reaction orders and KIE values were obtained for **3** as well, and yielded similar results (Figures S11 and S13). With these results in hand, one can say that the semi-hydrogenation of alkynes on the Pd-$(CaCO_3)_n$ catalyst is controlled, in the presence of adsorbed alkyne [83], by the H_2 splitting step over the Pd species. Were the hydrogen insertion/reductive elimination the limiting step, one would expect an inverse effect [84]. Given that the dissociation of H_2 limits the reaction rate, we attribute the Hammett plot results above to the fact that both the more electronically dense and the more charge depleted alkyne groups facilitate an heterolytic H_2 splitting by providing the right electronics, in accordance with the concave shape of the plot. This mechanism [79] has been observed before on nitrogen-functionalized Au heterogeneous catalysts during alkyne semi-hydrogenations [85] and Pd_1/TiO_2 hydrogenation reactions [86]. Illustrating it through a simplified model (Figure S16), one can

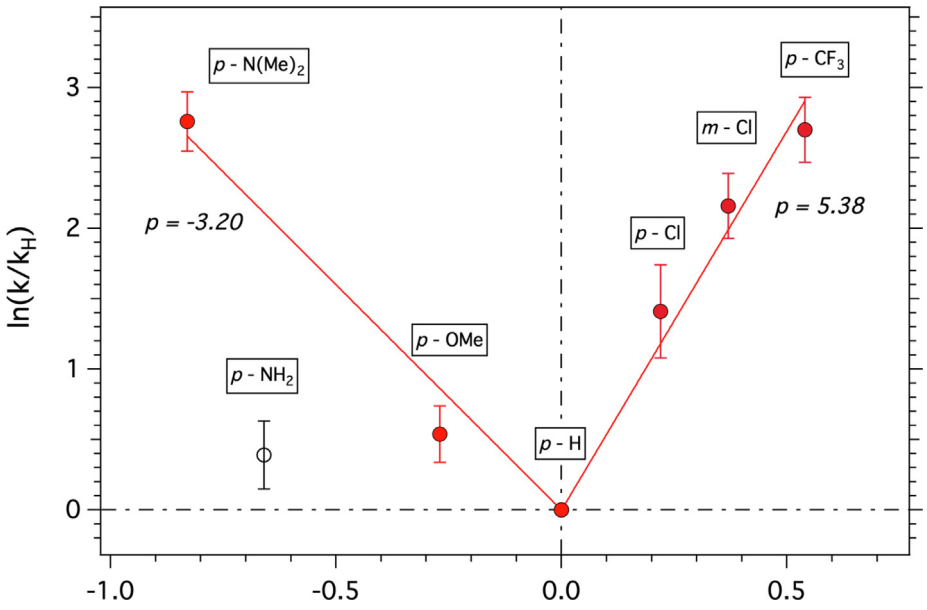

Fig. 6. Hammett plot for the hydrogenation of substituted aromatic alkynes catalyzed with Pd-$(CaCO_3)_n$.

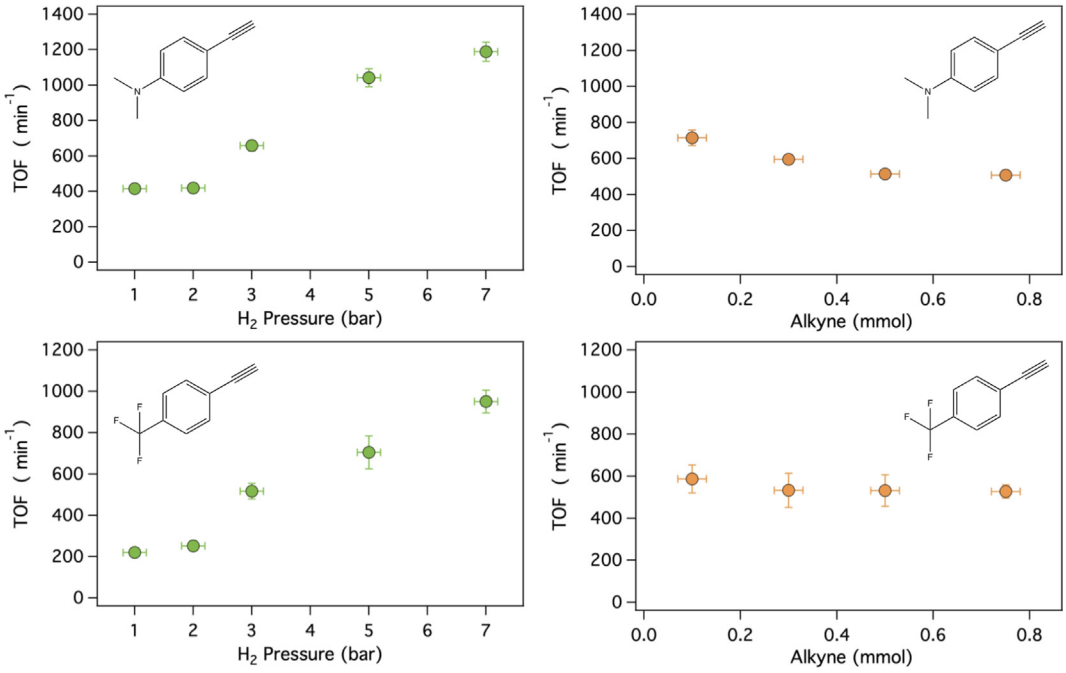

Fig. 7. Reaction rate dependence on alkyne concentration (left) and H_2 pressure (right) for selected substrates from the Hammett Plot in the two opposite mechanistic regimes, 1-ethynyl-4-dimethylaniline **7** and 4-trifluoromethylphenylacetylene **11**.

see that the Pd-$(CaCO_3)_n$ catalytic sites possess the ability to accommodate both the $H^{(\delta-)}$ or $H^{(\delta+)}$ counterparts, depending on the alkyne which they are interacting with. The ambivalence of the $Pd^{\delta+} - H^{\delta-}$ / $Pd^{\delta-} - H^{\delta+}$ bond has been demonstrated, although to our knowledge it has only been employed to understand the mechanism and regioselectivity of hydrogenation and isomerization of alkenes with organometallic catalysts [87,88]. More specifically, the authors found that when the reactive double bond was conjugated to an EWG, the H insertion occurred on the charge deficient carbon, implying a $Pd^{\delta+} - H^{\delta-}$ bond, while when conjugated to an EDG, the insertion occurred on the electronically rich carbon, implying a $Pd^{\delta-} - H^{\delta+}$ bond. As aforementioned, and in contrast to the case at hand, the hydrogenation rates of the reactions mediated by the Lindlar catalyst have been reported to remain constant regardless of the substrate charge [79]. From our understanding, the fact that the adsorbates on the Pd species of the Pd-$(CaCO_3)_n$ catalyst are able to tune the electronic environment of the active site, but are not able to do so on the Lindlar catalyst, is a consequence of the different metal particle size of each catalyst or, more specifically, the ability of larger metallic particles to disperse the effects of localized charges on the surface inwards, while smaller clusters must accommodate them on the surface itself.

3.4. Computational studies

As the resolution of sub-nano clusters at an atomistic level remains evasive for experimental techniques, theory might contribute to provide valuable insights into the catalytic mechanism. Our computational efforts have been focused on the precursor cluster, e.g., Pd-$(CaCO_3)_3$. As illustrated in Fig. 8 (left panel), two strategies are implemented to yield to reliable structures. The first approach uses the isolated components of the cluster. Atoms are combined to generate random combinations without imposing any initial bond order [40–42]. In the second method, we used the available $(CaCO_3)_3$ structure [43] to search for the most stable cluster at DFT-D level [44–48]. We have not included supports such as alumina in the computational studies, since we have observed that the alumina support does not notably hinder nor enhance the performance of the reaction, as shown in the results above for the hydrogenation reactions of **3** with supported and unsupported Pd-$CaCO_3$ clusters. These results led to assume that there was not a significant alumina-carbonate interaction, or at least that the alumina does not play a significant role in the catalytic process beyond supporting the catalytic sites. This assumption has chemical sense since carbonates are much stronger bases/nucleophiles than alumina.

Fig. 8 (right panel) includes the produced skeletons with the lowest energies. Our models suggest that Pd is efficiently integrated into the parent $(CaCO_3)_3$ cluster without distorting the original network; CO_3 anions originally connecting Ca cations are observed to simultaneously anchoring Pd through O–Pd contacts upon metal coordination. As results, four structures are localized in energetic window of 7.61 kcal/mol. Of course, there are other compatible structures in which atoms are organized without preserving the CO_3 entities. A close inspection of the last cluster depicted in Fig. 8 reveals the presence of CO_2 and –O–O– motifs (Figure S17). However, such less classical trends are associated with large relative energies (ΔE > 86.80 kcal/mol). One might expect to find the most favorable geometries under experimental conditions. Accordingly, the best ranked Pd-$(CaCO_3)_3$ nanocluster (Fig. 8, top structure on right panel) is retained in the computational protocol as the model to mimic the adsorption and catalytic phenomena.

Alkynes **1** and **4** are selected as representative species with large and small TOFs values, respectively. According to the results summarized in Fig. 9, a contrasting behavior occurs depending on the groups that sandwich the alkyne. On the one side, alkyne **1** is better adsorbed in the surface of the Pd-$(CaCO_3)_n$ cluster, with an interaction energy of −50.34 kcal/mol, significantly larger than the one predicted for alkyne **4** counterpart (-30.74 kcal/mol). The analysis of non-covalent interactions [49,50] hints that the presence of adjacent hydroxyl groups enables non-covalent bonds with CO_3^{2-} and Ca^{2+}, which explains that difference of ca. 10 kcal/mol (Figure S18). On the other hand, these additional contacts do not only better anchor alkyne **1** compared to **4**, but also have an impact on the adsorbate geometry. If we compare the optimized clusters before and after hydrogenation (marked with a vertical blue line), we can observe that the adsorption of alkyne **1** is fully compatible with the entry of H_2 into the Pd sphere of coordination. A contrast picture is foreseen for alkyne **4,** that interacts with Pd in a perpendicular manner and 'hides' the metallic center for the hydrogenation site (Figure S19). These accumulated evidences rationalize the positive effect of hydroxyl groups in the reaction rates.

Molecular models also help to monitor the semi-hydrogenation mechanism. The energetic profiles plotted in Fig. 9 are associated to a step-wise mechanism, e.g., hydrogen atoms are transferred to the alkyne through two transition states (TS1 and TS2) and do not follow a concerted mechanism (videos S1–S2). It should be stressed that after the adsorption of H_2, the energetic profile for alkyne **4** becomes flatter (more favorable) compared to **1**. The former shows smaller energetic barrier for the transference of both the first and second hydrogen atoms (see TS1 and TS2 relative energies). The same apply for the final energy of the semi-hydrogenated alkyne: −48.45 kcal/mol (alkyne **4**) vs. −35.96 kcal/mol (alkyne **1**).

Numeric outcomes demonstrate how the structure is critical to better accommodate internal alkynes onto the cluster. Decoration with hydroxyl groups helps to fold the alkyne towards the surface of the Pd-$(CaCO_3)_3$ cluster, which in turn keep the catalytic Pd-site exposed for the concomitant coordination of H_2 to the cluster. Alkynes without such interaction ability are expected to interact with Pd in the same catalytic region required for the H_2 coordination. We must conclude that earlier stage (adsorption step of the

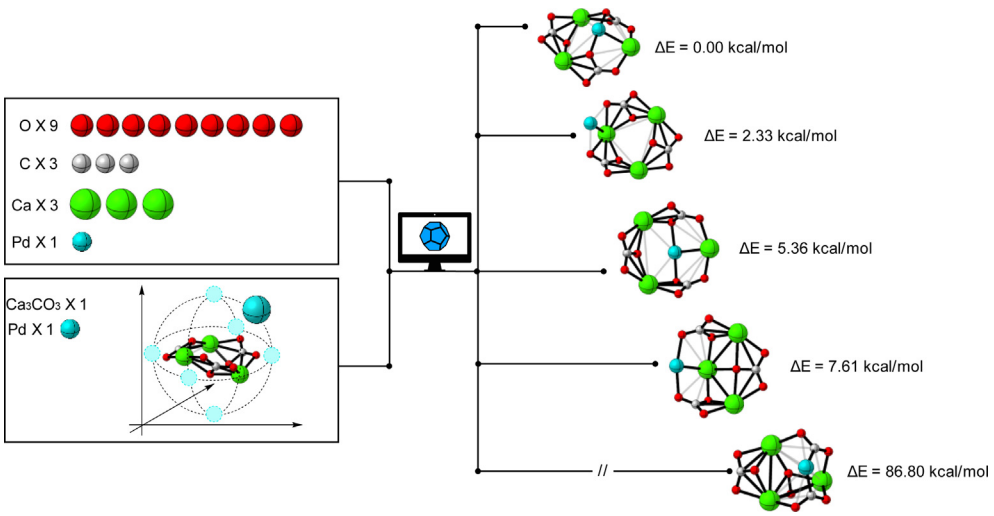

Fig. 8. Left panel: initial model systems. From top to bottom: unbiased structure search based on the chemical composition without assumptions about the cluster structure; optimization of the $(CaCO_3)_3$ cluster upon complexation with a Pd atom. Right panel: predicted structures for the lowest energy Pd-$(CaCO_3)_3$ clusters and their relative energies (in kcal/mol).

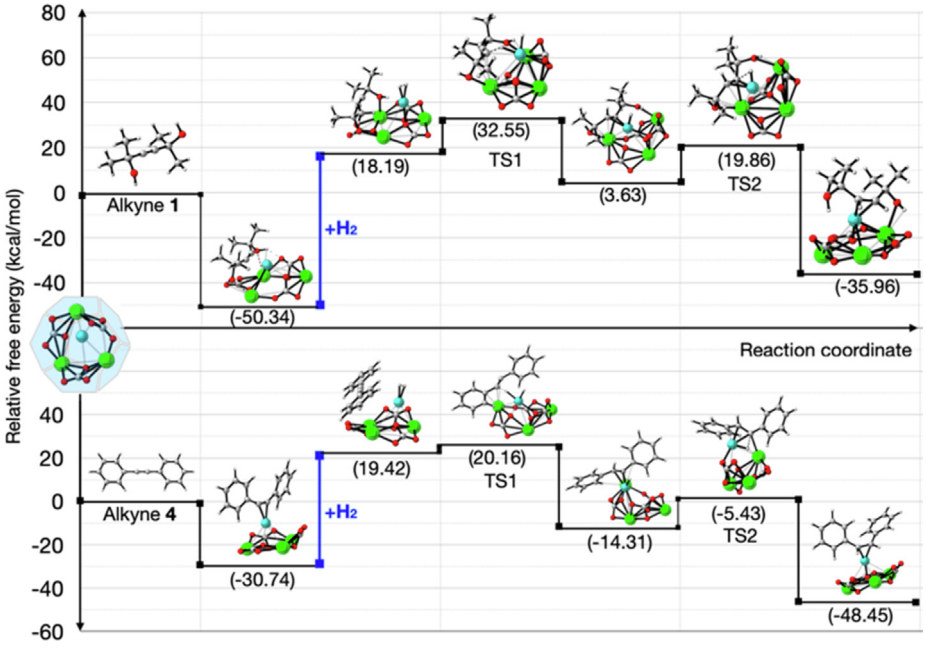

Fig. 9. Reaction coordinate analysis and optimized structures for the semi-hydrogenation of alkynes **1** and **4**. The calculated relative free energies are given in kcal/mol. For the sake of clarity, both profiles are plotted with the same energetic scale. Hydrogens are displayed as white spheres. The rest of atomic color scheme is consistent with Fig. 8.

substrate on the surface of the catalyst, previous to the hydrogen splitting and hydrogen insertions) plays a critical role in the global reaction rate. It is true that participation of distorted Pd cluster structures might play a role here, and this approach deserves further studies in the future [89–92].

3.5. Applied industrial chemistry

Considering the results of the reaction scope, and our insights on the reaction mechanism, the novel catalyst has the potential to excel in the synthesis of some industrially relevant alkenes, which result from the semi-hydrogenation of alkynols or internal alkynes. The selective hydrogenations of four distinct substrates with these functionalities have been selected to showcase the performance of the Pd-$(CaCO_3)_n$ catalyst: i) TMDD (2,4,7,9-tetramethyl-5-decyn-4,7-diol) **31**, a *gemini* surfactant, ii) 5-decynylacetate **33**, to give a typical long chain olefin structure such as *cis*-5-decenylacetate (Z5-10Ac) **34**, appearing in insect sex pheromones used in sustainable pesticides [93,94], iii) dehydrolinalool (DHL) **35**, a widely used terpene for the synthesis of fragrances [13], and iv) MBY (2-methyl-3-butyn-2-ol) **37** to produce the corresponding alkene (MBE) **38**, used in the synthesis of vitamins A and E, as well as in the fragrance industry as a reaction intermediate [13].

The results in Fig. 10 show that, indeed, the performance of the Pd-$(CaCO_3)_n$ catalyst was excellent for internal alkynes, with complete conversions and very high selectivities towards the desired alkene. The formation of linalool, while being slower, as expected for a terminal alkyne, was highly selective and showcased the affinity of the catalyst for homopropargyl groups in competitive intramolecular hydrogenations. Similarly, the hydrogenation of MBY was fast and highly selective, with total conversion after approximately 2 h and, with H_2 still present, selectivity barely decreased for the next 2 h.

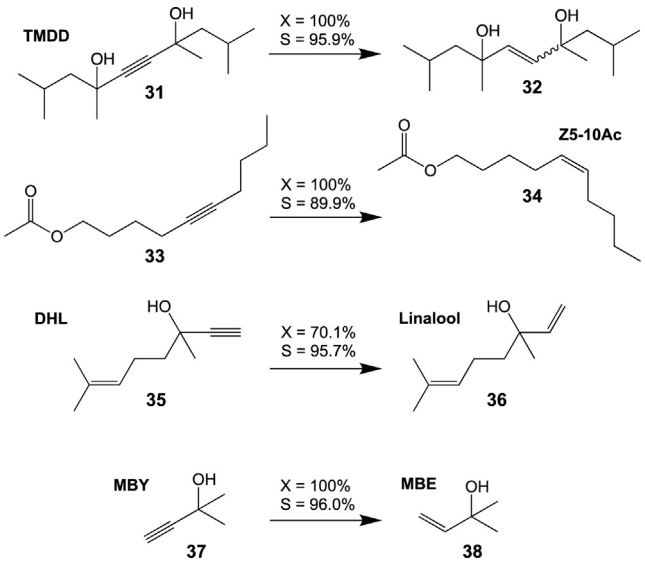

Fig. 10. Alkyne conversions and selectivities with Pd-$(CaCO_3)_n$ catalyst (0.46 ppm Pd) for the formation of 2,4,7,9-tetramethyl-5-decene-4,7-diol **32**, 5-decenylacetate **34** and linalool **36**, reaction conditions: 333 K, 20 h reaction time, 0.15 mmol alkyne and 0.5 mL of ethanol; and the formation of 2-methyl-3-buten-2-ol (MBE) **38**, reaction conditions: 333 K, 4 h reaction time, 0.3 mmol alkyne and 0.5 mL of ethanol.

4. Conclusions

Pd-$(CaCO_3)_n$ clusters of just few atoms have been synthesized and used as a catalyst for the semi-hydrogenation reaction of alkynes. Either in solution or supported, the clusters show a catalytic activity and selectivity, particularly for internal alkynes, one order of magnitude higher than typical commercial catalysts, including the parent Lindlar catalyst. Mechanistic studies support a flexible catalytic operativity of the Pd-$(CaCO_3)_n$ clusters by means of the concomitant action of Pd and carbonate, particularly propargyl alcohols [16,86,95] to hydrogenate selectively alkynes with a wide steric and electronic spectrum. These results open the way to synthesize highly active and selective molecular catalysts inspired by the active centers (“minimum catalytic unit”) of extended solid catalysts.

Declaration of Competing Interest

The authors declare that they have no known competing financial interests or personal relationships that could have appeared to influence the work reported in this paper.

Acknowledgements

This work is part of the projects PID2020–115100GB–I00 and PID2019–107578GA–I00, both funded by MCIN/AEI/10.13039/501100011033MICIIN, and "La Caixa" Foundation grant (ID 100010434), code LCF/BQ/DI19/11730029. AC–STEM data were obtained at DME–UCA node of the Spanish Unique Scientific and Technological Infrastructure (ICTS) of Electron Microscopy of Materials ELECMIM. This work used computational facilities from the Plataforma Andaluza de Bioinformática installed at the Universidad de Málaga.

Appendix A. Supplementary data

Supplementary data to this article can be found online at https://doi.org/10.1016/j.jcat.2022.02.020.

References

[1] L. Liu, A. Corma, Metal Catalysts for Heterogeneous Catalysis: From Single Atoms to Nanoclusters and Nanoparticles, Chem. Rev. 118 (10) (2018) 4981–5079, https://doi.org/10.1021/acs.chemrev.7b00776.
[2] A. Leyva-Pérez, P. García-García, A. Corma, Multisite organic-inorganic hybrid catalysts for the direct sustainable synthesis of GABAergic drugs, Angew. Chem. - Int. Ed. 53 (33) (2014) 8687–8690, https://doi.org/10.1002/anie.201403049.
[3] W. Long, N.A. Brunelli, S.A. Didas, E.W. Ping, C.W. Jones, Aminopolymer-silica composite-supported Pd catalysts for selective hydrogenation of alkynes, ACS Catal. 3 (8) (2013) 1700–1708, https://doi.org/10.1021/cs3007395.
[4] Y. Kuwahara, H. Kango, H. Yamashita, Pd Nanoparticles and Aminopolymers Confined in Hollow Silica Spheres as Efficient and Reusable Heterogeneous Catalysts for Semihydrogenation of Alkynes, ACS Catal. 9 (3) (2019) 1993–2006, https://doi.org/10.1021/acscatal.8b0465310.1021/acscatal.8b04653.s001.
[5] S. Mitchell, R. Qin, N. Zheng, J. Pérez-Ramírez, Nanoscale engineering of catalytic materials for sustainable technologies, Nat. Nanotechnol. 16 (2) (2021) 129–139, https://doi.org/10.1038/s41565-020-00799-8.
[6] Z. Jin, A.J. Bard, Atom-by-atom electrodeposition of single isolated cobalt oxide molecules and clusters for studying the oxygen evolution reaction, Proc. Natl. Acad. Sci. U. S. A. 117 (23) (2020) 12651–12656, https://doi.org/10.1073/pnas.2002168117.
[7] D. Albani, M. Shahrokhi, Z. Chen, S. Mitchell, R. Hauert, N. López, J. Pérez-ramírez, Selective ensembles in supported palladium sulfide nanoparticles for alkyne semi-hydrogenation, Nat. Commun. (2018) 1–11, https://doi.org/10.1038/s41467-018-05052-4.
[8] K. Saika, M. Yoshida, A minimum catalytic unit of F1-ATPase shows non-cooperative ATPase activity inherent in a single catalytic site with a Km 70 μM, FEBS Lett. 368 (1995) 207–210, https://doi.org/10.1016/0014-5793(95)00644-O.
[9] E. Cid, R.A. Geremia, J.J. Guinovart, J.C. Ferrer, Glycogen synthase: Towards a minimum catalytic unit?, FEBS Lett 528 (2002) 5–11, https://doi.org/10.1016/S0014-5793(02)03313-6.
[10] J. Vionnet, E.S. Kempner, W.F. Vann, Functional molecular mass of Escherichia coli K92 polysialyltransferase as determined by radiation target analysis, Biochemistry 45 (45) (2006) 13511–13516, https://doi.org/10.1021/bi061486k.
[11] O. Lazarus, T.W. Woolerton, A. Parkin, M.J. Lukey, E. Reisner, J. Seravalli, E. Pierce, S.W. Ragsdale, F. Sargent, F.A. Armstrong, Water-gas shift reaction catalyzed by redox enzymes on conducting graphite platelets, J. Am. Chem. Soc. 131 (40) (2009) 14154–14155, https://doi.org/10.1021/ja905797w.
[12] G. Vilé, N. Almora-Barrios, S. Mitchell, N. López, J. Pérez-Ramírez, From the lindlar catalyst to supported ligand-modified palladium nanoparticles: Selectivity patterns and accessibility constraints in the continuous-flow three-phase hydrogenation of acetylenic compounds, Chem. – A Eur. J. 20 (20) (2014) 5926–5937, https://doi.org/10.1002/chem.201304795.
[13] W. Bonrath, J. Medlock, J. Schütz, B. Wüstenberg, T. Netscher, Chapter 3: Hydrogenation in the Vitamins and Fine Chemicals Industry – An Overview, Hydrogenation (2016) 69–90.
[14] P. Ertl, T. Schuhmann, A Systematic Cheminformatics Analysis of Functional Groups Occurring in Natural Products, J. Nat. Prod. 82 (5) (2019) 1258–1263, https://doi.org/10.1021/acs.jnatprod.8b0102210.1021/acs.jnatprod.8b01022.s001.
[15] A.J. Smaligo, J. Wu, N.R. Burton, A.S. Hacker, A.C. Shaikh, J.C. Quintana, R. Wang, C. Xie, O. Kwon, Oxodealkenylative Cleavage of Alkene C(sp3)−C(sp2) Bonds: A Practical Method for Introducing Carbonyls into Chiral Pool Materials, Angew. Chem. - Int. Ed. 59 (3) (2020) 1211–1215, https://doi.org/10.1002/anie.201913201.
[16] M. Tejeda-Serrano, M. Mon, B. Ross, F. Gonell, J. Ferrando-Soria, A. Corma, A. Leyva-Pérez, D. Armentano, E. Pardo, Isolated Fe(III)-O Sites Catalyze the Hydrogenation of Acetylene in Ethylene Flows under Front-End Industrial Conditions, J. Am. Chem. Soc. 140 (28) (2018) 8827–8832, https://doi.org/10.1021/jacs.8b0466910.1021/jacs.8b04669.s00110.1021/jacs.8b04669.s002.
[17] S. Furukawa, T. Komatsu, Selective Hydrogenation of Functionalized Alkynes to (E) – Alkenes, Using Ordered Alloys as Catalysts, ACS Catal. 6 (3) (2016) 2121–2125, https://doi.org/10.1021/acscatal.5b0295310.1021/acscatal.5b02953.s001.
[18] P.W. Albers, K. Möbus, C.D. Frost, S.F. Parker, Characterization of β-palladium hydride formation in the lindlar catalyst and in carbon-supported palladium, J. Phys. Chem. C. 115 (50) (2011) 24485–24493, https://doi.org/10.1021/jp205951c.
[19] M. García-Mota, B. Bridier, J. Pérez-Ramírez, N. López, Interplay between carbon monoxide, hydrides, and carbides in selective alkyne hydrogenation on palladium, J. Catal. 273 (2) (2010) 92–102, https://doi.org/10.1016/j.jcat.2010.04.018.
[20] M.W. Tew, M. Janousch, T. Huthwelker, J.A. van Bokhoven, The roles of carbide and hydride in oxide-supported palladium nanoparticles for alkyne hydrogenation, J. Catal. 283 (1) (2011) 45–54, https://doi.org/10.1016/j.jcat.2011.06.025.
[21] A.L. Bugaev, O.A. Usoltsev, A.A. Guda, K.A. Lomachenko, I.A. Pankin, Y.V. Rusalev, H. Emerich, E. Groppo, R. Pellegrini, A.V. Soldatov, J.A. van Bokhoven, C. Lamberti, Palladium Carbide and Hydride Formation in the Bulk and at the Surface of Palladium Nanoparticles, J. Phys. Chem. C. 122 (22) (2018) 12029–12037, https://doi.org/10.1021/acs.jpcc.7b1147310.1021/acs.jpcc.7b11473.s001.
[22] T. Fukuda, Partial Hydrogenation of 1,4-Butynediol. II. On the Role of Calcium Carbonate as a Carrier of the Palladium Catalyst, Bull. Chem. Soc. Jpn. 31 (3) (1958) 343–347, https://doi.org/10.1246/bcsj.31.343.
[23] P.T. Witte, P.H. Berben, S. Boland, J.G. Donkervoort, BASF NanoSelect TM Technology : Innovative Supported Pd- and Pt-based Catalysts for Selective Hydrogenation Reactions, Top. Catal. 55 (2012) 505–511, https://doi.org/10.1007/s11244-012-9818-y.
[24] J.A. Delgado, O. Benkirane, C. Claver, D. Curulla-Ferré, C. Godard, Advances in the preparation of highly selective nanocatalysts for the semi-hydrogenation of alkynes using colloidal approaches, Dalt. Trans. 46 (37) (2017) 12381–12403.
[25] N. López, C. Vargas-Fuentes, Promoters in the hydrogenation of alkynes in mixtures: Insights from density functional theory, Chem. Commun. 48 (10) (2012) 1379–1391.
[26] B. Bridier, N. López, J. Pérez-Ramírez, Molecular understanding of alkyne hydrogenation for the design of selective catalysts, Dalt. Trans. 39 (2010) 8363–8376, https://doi.org/10.1039/c001226b.
[27] C.W.A. Chan, A.H. Mahadi, M.M.J. Li, E.C. Corbos, C. Tang, G. Jones, W.C.H. Kuo, J. Cookson, C.M. Brown, P.T. Bishop, S.C.E. Tsang, Interstitial modification of palladium nanoparticles with boron atoms as a green catalyst for selective hydrogenation, Nat. Commun. 5 (2014) 1–10, https://doi.org/10.1038/ncomms6787.
[28] Y. Liu, A.J. McCue, C. Miao, J. Feng, D. Li, J.A. Anderson, Palladium phosphide nanoparticles as highly selective catalysts for the selective hydrogenation of acetylene, J. Catal. 364 (2018) 406–414, https://doi.org/10.1016/j.jcat.2018.06.001.
[29] K.C.K. Swamy, A.S. Reddy, K. Sandeep, A. Kalyani, Advances in chemoselective and/or stereoselective semihydrogenation of alkynes, Tetrahedron Lett. 59 (5) (2018) 419–429, https://doi.org/10.1016/j.tetlet.2017.12.057.
[30] A. Papp, Á. Molnár, Á. Mastalir, Catalytic investigation of Pd particles supported on MCM-41 for the selective hydrogenations of terminal and internal alkynes, Appl. Catal. A Gen. 289 (2) (2005) 256–266, https://doi.org/10.1016/j.apcata.2005.05.007.
[31] S. Yang, C. Cao, L.i. Peng, J. Zhang, B. Han, W. Song, A Pd-Cu2O nanocomposite as an effective synergistic catalyst for selective semi-hydrogenation of the terminal alkynes only, Chem. Commun. 52 (18) (2016) 3627–3630.
[32] Y.e. Lu, X. Feng, B.S. Takale, Y. Yamamoto, W. Zhang, M. Bao, Highly Selective Semihydrogenation of Alkynes to Alkenes by Using an Unsupported Nanoporous Palladium Catalyst: No Leaching of Palladium into the Reaction Mixture, ACS Catal. 7 (12) (2017) 8296–8303, https://doi.org/10.1021/acscatal.7b0291510.1021/acscatal.7b02915.s001.
[33] S. Lee, S.-J. Shin, H. Baek, Y. Choi, K. Hyun, M. Seo, K. Kim, D.-Y. Koh, H. Kim, M. Choi, Dynamic metal-polymer interaction for the design of chemoselective and long-lived hydrogenation catalysts, Sci. Adv. 6 (28) (2020), https://doi.org/10.1126/sciadv.abb7369.
[34] E.D. Slack, C.M. Gabriel, B.H. Lipshutz, A palladium nanoparticle-nanomicelle combination for the stereo-selective semihydrogenation of alkynes in water at room temperature, Angew. Chem. - Int. Ed. 53 (51) (2014) 14051–14054, https://doi.org/10.1002/anie.201407723.
[35] R. Maazaoui, R. Abderrahim, F. Chemla, F. Ferreira, A. Perez-Luna, O. Jackowski, Catalytic Chemoselective and Stereoselective Semihydrogenation of Alkynes to E-Alkenes Using the Combination of Pd Catalyst and ZnI 2, Org. Lett. 20 (23) (2018) 7544–7549, https://doi.org/10.1021/acs.orglett.8b0329510.1021/acs.orglett.8b03295.s001.

[36] D. Gebauer, A. Völkel, H. Cölfen, Antje Völkel, Stable Prenucleation Calcium Carbonate Clusters, Science (80-) 322 (5909) (2008) 1819–1822.

[37] D. Palin, R.W. Style, J. Zlopaša, J.J. Petrozzini, M.A. Pfeifer, H.M. Jonkers, E.R. Dufresne, L.A. Estroff, Forming Anisotropic Crystal Composites: Assessing the Mechanical Translation of Gel Network Anisotropy to Calcite Crystal Form, J. Am. Chem. Soc. 143 (9) (2021) 3439–3447, https://doi.org/10.1021/jacs.0c1232610.1021/jacs.0c12326.s001.

[38] S. Ida, N. Kim, E. Ertekin, S. Takenaka, T. Ishihara, Photocatalytic reaction centers in two-dimensional titanium oxide crystals, J. Am. Chem. Soc. 137 (1) (2015) 239–244, https://doi.org/10.1021/ja509970z.

[39] M.i. Peng, C. Dong, R. Gao, D. Xiao, H. Liu, D. Ma, Fully exposed cluster catalyst (FECC): Toward rich surface sites and full atom utilization efficiency, ACS Cent. Sci. 7 (2) (2021) 262–273, https://doi.org/10.1021/acscentsci.0c01486.

[40] Y. Wang, J. Lv, L. Zhu, Y. Ma, Crystal structure prediction via particle-swarm optimization, Phys. Rev. B - Condens. Matter Mater. Phys. 82 (2010) 1–8, https://doi.org/10.1103/PhysRevB.82.094116.

[41] Y. Wang, J. Lv, L.i. Zhu, Y. Ma, CALYPSO: A method for crystal structure prediction, Comput. Phys. Commun. 183 (10) (2012) 2063–2070, https://doi.org/10.1016/j.cpc.2012.05.008.

[42] J. Lv, Y. Wang, L. Zhu, Y. Ma, Particle-swarm structure prediction on clusters, J. Chem. Phys. 137 (2012) 1–8, https://doi.org/10.1063/1.4746757.

[43] M. Chen, A.S. McNeill, Y. Hu, D.A. Dixon, Elucidation of Bottom-Up Growth of CaCO3 Involving Prenucleation Clusters from Structure Predictions and Decomposition of Globally Optimized (CaCO3)n Nanoclusters, ACS Nano. 14 (4) (2020) 4153–4165, https://doi.org/10.1021/acsnano.9b0890710.1021/acsnano.9b08907.s001.

[44] M.J. Frisch, G.W. Trucks, H.B. Schlegel, G.E. Scuseria, M.A. Robb, J.R. Cheeseman, G. Scalmani, V. Barone, G.A. Petersson, H. Nakatsuji, X. Li, M. Caricato, A.V. Marenich, J. Bloino, B.G. Janesko, R. Gomperts, B. Mennucci, H.P. Hratchian, J.V. Ortiz, A.F. Izmaylov, J.L. Sonnenberg, D. Williams-Young, F. Ding, F. Lipparini, F. Egidi, J. Goings, B. Peng, A. Petrone, T. Henderson, D. Ranasinghe, V.G. Zakrzewski, J. Gao, N. Rega, G. Zheng, W. Liang, M. Hada, M. Ehara, K. Toyota, R. Fukuda, J. Hasegawa, M. Ishida, T. Nakajima, Y. Honda, O. Kitao, H. Nakai, T. Vreven, K. Throssell, J.A. Montgomery Jr., J.E. Peralta, F. Ogliaro, M.J. Bearpark, J.J. Heyd, E.N. Brothers, K.N. Kudin, V.N. Staroverov, T.A. Keith, R. Kobayashi, J. Normand, K. Raghavachari, A.P. Rendell, J.C. Burant, S.S. Iyengar, J. Tomasi, M. Cossi, J.M. Millam, M. Klene, C. Adamo, R. Cammi, J.W. Ochterski, R. L. Martin, K. Morokuma, O. Farkas, J.B. Foresman, D.J. Fox, Gaussian 16, Revision C.01, Gaussian, Inc., Wallingford CT, 2016.

[45] J. Da Chai, M. Head-Gordon, Long-range corrected hybrid density functionals with damped atom-atom dispersion corrections, Phys. Chem. Chem. Phys. 10 (2008) 6615–6620, https://doi.org/10.1039/b810189b.

[46] F. Weigend, R. Ahlrichs, Balanced basis sets of split valence, triple zeta valence and quadruple zeta valence quality for H to Rn: Design and assessment of accuracy, Phys. Chem. Chem. Phys. 7 (2005) 3297–3305, https://doi.org/10.1039/b508541a.

[47] F. Weigend, Accurate Coulomb-fitting basis sets for H to Rn, Phys. Chem. Chem. Phys. 8 (2006) 1057–1065, https://doi.org/10.1039/b515623h.

[48] J. Tomasi, B. Mennucci, R. Cammi, Quantum mechanical continuum solvation models, Chem. Rev. 105 (8) (2005) 2999–3094, https://doi.org/10.1021/cr9904009.

[49] E.R. Johnson, S. Keinan, P. Mori-Sánchez, J. Contreras-García, A.J. Cohen, W. Yang, Revealing noncovalent interactions, J. Am. Chem. Soc. 132 (18) (2010) 6498–6506, https://doi.org/10.1021/ja100936w.

[50] J. Contreras-García, E.R. Johnson, S. Keinan, R. Chaudret, J.-P. Piquemal, D.N. Beratan, W. Yang, NCIPLOT: A program for plotting noncovalent interaction regions, J. Chem. Theory Comput. 7 (3) (2011) 625–632, https://doi.org/10.1021/ct100641a.

[51] Jaguar, version 11.1, Schrodinger, Inc., New York, NY, 2021.

[52] A.D. Bochevarov, E. Harder, T.F. Hughes, J.R. Greenwood, D.A. Braden, D.M. Philipp, D. Rinaldo, M.D. Halls, J. Zhang, R.A. Friesner, Jaguar: A high-performance quantum chemistry software program with strengths in life and materials sciences, Int. J. Quantum Chem. 113 (18) (2013) 2110–2142, https://doi.org/10.1002/qua.24481.

[53] S.S. Zalesskiy, V.P. Ananikov, $Pd_2(dba)_3$ as a precursor of soluble metal complexes and nanoparticles: Determination of palladium active species for catalysis and synthesis, Organometallics 31 (6) (2012) 2302–2309, https://doi.org/10.1021/om201217r.

[54] Z. Liu, C. Shao, B. Jin, Z. Zhang, Y. Zhao, X. Xu, R. Tang, Crosslinking ionic oligomers as conformable precursors to calcium carbonate, Nature 574 (7778) (2019) 394–398, https://doi.org/10.1038/s41586-019-1645-x.

[55] M. Kellermeier, D. Gebauer, E. Melero-García, M. Drechsler, Y. Talmon, L. Kienle, H. Cölfen, J.M. García-Ruiz, W. Kunz, Colloidal Stabilization of Calcium Carbonate Prenucleation Clusters with Silica, Adv. Funct. Mater. 22 (20) (2012) 4301–4311, https://doi.org/10.1002/adfm.201200953.

[56] W. Chen, W. Cai, Y. Lei, L. Zhang, A sonochemical approach to the confined synthesis of palladium nanoparticles in mesoporous silica, Mater. Lett. 50 (2-3) (2001) 53–56, https://doi.org/10.1016/S0167-577X(00)00411-0.

[57] J. Cookson, The preparation of palladium nanoparticles, Platin. Met. Rev. 56 (2012) 83–98, https://doi.org/10.1595/147106712X632415.

[58] A. Nemamcha, J.-L. Rehspringer, D. Khatmi, Synthesis of palladium nanoparticles by sonochemical reduction of palladium(II) nitrate in aqueous solution, J. Phys. Chem. B 110 (1) (2006) 383–387, https://doi.org/10.1021/jp0535801.

[59] L. Xu, X.-C. Wu, J.-J. Zhu, Green preparation and catalytic application of Pd nanoparticles, Nanotechnology 19 (30) (2008) 305603, https://doi.org/10.1088/0957-4484/19/30/305603.

[60] A. Sandell, J. Libuda, P.A. Brühwiler, S. Andersson, A.J. Maxwell, M. Bäumer, N. Mårtensson, H.J. Freund, Interaction of CO with Pd clusters supported on a thin alumina film, J. Vac. Sci. Technol. A Vacuum, Surfaces, Film. 14 (3) (1996) 1546–1551, https://doi.org/10.1116/1.580293.

[61] M. Brun, A. Berthet, J.C. Bertolini, XPS, AES and Auger parameter of Pd and PdO, J. Electron Spectros. Relat. Phenomena. 104 (1-3) (1999) 55–60.

[62] G. Vilé, D. Albani, M. Nachtegaal, Z. Chen, D. Dontsova, M. Antonietti, N. López, J. Pérez-Ramírez, A Stable Single-Site Palladium Catalyst for Hydrogenations, Angew. Chem. - Int. Ed. 54 (38) (2015) 11265–11269, https://doi.org/10.1002/anie.201505073.

[63] Z. Chen, E. Vorobyeva, S. Mitchell, E. Fako, N. López, S.M. Collins, R.K. Leary, P.A. Midgley, R. Hauert, J. Pérez-Ramírez, Single-atom heterogeneous catalysts based on distinct carbon nitride scaffolds, Natl. Sci. Rev. 5 (2018) 642–652, https://doi.org/10.1093/nsr/nwy048.

[64] E. Fernández, M.A. Rivero-Crespo, I. Domínguez, P. Rubio-Marqués, J. Oliver-Meseguer, L. Liu, M. Cabrero-Antonino, R. Gavara, J.C. Hernández-Garrido, M. Boronat, A. Leyva-Pérez, A. Corma, Base-Controlled Heck, Suzuki, and Sonogashira Reactions Catalyzed by Ligand-Free Platinum or Palladium Single Atom and Sub-Nanometer Clusters, J. Am. Chem. Soc. 141 (5) (2019) 1928–1940, https://doi.org/10.1021/jacs.8b0788410.1021/jacs.8b07884.s001.

[65] Z. Li, Q. Ren, X. Wang, W. Chen, L. Leng, M. Zhang, J.H. Horton, B.o. Liu, Q. Xu, W. Wu, J. Wang, Highly Active and Stable Palladium Single-Atom Catalyst Achieved by a Thermal Atomization Strategy on an SBA-15 Molecular Sieve for Semi-Hydrogenation Reactions, ACS Appl. Mater. Interfaces. 13 (2) (2021) 2530–2537, https://doi.org/10.1021/acsami.0c1757010.1021/acsami.0c17570.s001.

[66] E. Tiburcio, R. Greco, M. Mon, J. Ballesteros-Soberanas, J. Ferrando-Soria, M. López-Haro, J.C. Hernández-Garrido, J. Oliver-Meseguer, C. Marini, M. Boronat, D. Armentano, A. Leyva-Pérez, E. Pardo, Soluble/MOF-Supported Palladium Single Atoms Catalyze the Ligand-, Additive-, and Solvent-Free Aerobic Oxidation of Benzyl Alcohols to Benzoic Acids, J. Am. Chem. Soc. 143 (6) (2021) 2581–2592, https://doi.org/10.1021/jacs.0c1236710.1021/jacs.0c12367.s001.

[67] P. Rubio-Marqués, M.A. Rivero-Crespo, A. Leyva-Pérez, A. Corma, Well-Defined Noble Metal Single Sites in Zeolites as an Alternative to Catalysis by Insoluble Metal Salts, J. Am. Chem. Soc. 137 (36) (2015) 11832–11837, https://doi.org/10.1021/jacs.5b07304.

[68] F.R. Fortea-Pérez, M. Mon, J. Ferrando-Soria, M. Boronat, A. Leyva-Pérez, A. Corma, J.M. Herrera, D. Osadchii, J. Gascon, D. Armentano, E. Pardo, The MOF-driven synthesis of supported palladium clusters with catalytic activity for carbene-mediated chemistry, Nat. Mater. 16 (7) (2017) 760–766, https://doi.org/10.1038/nmat4910.

[69] F. Garnes-Portolés, R. Greco, J. Oliver-Meseguer, J. Castellanos-Soriano, M. Consuelo Jiménez, M. López-Haro, J.C. Hernández-Garrido, M. Boronat, R. Pérez-Ruiz, A. Leyva-Pérez, Regioirregular and catalytic Mizoroki-Heck reactions, Nat. Catal. 4 (4) (2021) 293–303, https://doi.org/10.1038/s41929-021-00592-3.

[70] N. Cherkasov, D.Y. Murzin, C.R.A. Catlow, A. Chutia, Selectivity of the Lindlar catalyst in alkyne semi-hydrogenation: a direct liquid-phase adsorption study, Catal. Sci. Technol. 11 (18) (2021) 6205–6216.

[71] E. Janusson, H.S. Zijlstra, P.P.T. Nguyen, L. MacGillivray, J. Martelino, J.S. McIndoe, Real-time analysis of Pd2(dba)3 activation by phosphine ligands, Chem. Commun. 53 (5) (2017) 854–856.

[72] T.A. Nijhuis, G. van Koten, J.A. Moulijn, Optimized palladium catalyst systems for the selective liquid-phase hydrogenation of functionalyzed alkynes, Appl. Catal. A Gen. 238 (2) (2003) 259–271, https://doi.org/10.1016/S0926-860X(02)00372-1.

[73] M. García-Mota, J. Gómez-Díaz, G. Novell-Leruth, C. Vargas-Fuentes, L. Bellarosa, B. Bridier, J. Pérez-Ramírez, N. López, A density functional theory study of the "mythic" Lindlar hydrogenation catalyst, Theor. Chem. Acc. 128 (4-6) (2011) 663–673, https://doi.org/10.1007/s00214-010-0800-0.

[74] J. Ballesteros-Soberanas, L.D. Ellis, J.W. Medlin, Effects of Phosphonic Acid Monolayers on the Dehydration Mechanism of Aliphatic Alcohols on TiO2, ACS Catal. 9 (9) (2019) 7808–7816, https://doi.org/10.1021/acscatal.9b0208210.1021/acscatal.9b02082.s001.

[75] G.X. Pei, X.Y. Liu, A. Wang, L. Li, Y. Huang, T. Zhang, J.W. Lee, B.W.L. Jang, C.Y. Mou, Promotional effect of Pd single atoms on Au nanoparticles supported on silica for the selective hydrogenation of acetylene in excess ethylene, New J. Chem. 38 (2014) 2043–2051, https://doi.org/10.1039/c3nj01136d.

[76] G.X. Pei, X.Y. Liu, A. Wang, A.F. Lee, M.A. Isaacs, L. Li, X. Pan, X. Yang, X. Wang, Z. Tai, K. Wilson, T. Zhang, Ag alloyed Pd single-atom catalysts for efficient selective hydrogenation of acetylene to ethylene in excess ethylene, ACS Catal. 5 (6) (2015) 3717–3725, https://doi.org/10.1021/acscatal.5b00700.

[77] G.C. Bond, Hydrogenation of alkynes, in: Met. React. Hydrocarb. Fundam. Appl. Catal., Springer, Boston, MA, 2005, pp. 395–435.

[78] J.B. Geri, J.T. York, A systematic examination of ligand basicity effects on bonding in palladium(0)- and palladium(II)-ethylene complexes, Inorganica Chim. Acta 483 (2018) 191–202, https://doi.org/10.1016/j.ica.2018.08.008.

[79] J.L. Fiorio, R.V. Gonçalves, E. Teixeira-Neto, M.A. Ortuño, N. López, L.M. Rossi, Accessing Frustrated Lewis Pair Chemistry through Robust Gold@N-Doped Carbon for Selective Hydrogenation of Alkynes, ACS Catal. 8 (4) (2018) 3516–3524, https://doi.org/10.1021/acscatal.8b0080610.1021/acscatal.8b00806.s001.

[80] H.M. Neu, T. Yang, R.A. Baglia, T.H. Yosca, M.T. Green, M.G. Quesne, S.P. de Visser, D.P. Goldberg, Oxygen-atom transfer reactivity of axially ligated mn (V)-oxo complexes: Evidence for enhanced electrophilic and nucleophilic pathways, J. Am. Chem. Soc. 136 (39) (2014) 13845–13852, https://doi.org/10.1021/ja507177h.
[81] P.D. Maria, A. Fontana, C. Gasbarri, G. Siani, P. Zanirato, G. Cirrincione, Kinetics of the Z-E isomerization of monosubstituted azobenzenes in polar organic and aqueous micellar solvents, Arkivoc 2009 (8) (2009) 16–29, https://doi.org/10.3998/ark.5550190.0010.803.
[82] X. Zhao, L. Zhou, W. Zhang, C. Hu, L. Dai, L. Ren, B. Wu, G. Fu, N. Zheng, Thiol Treatment Creates Selective Palladium Catalysts for Semihydrogenation of Internal Alkynes, Chem 4 (5) (2018) 1080–1091, https://doi.org/10.1016/j.chempr.2018.02.011.
[83] M. Tejeda-Serrano, J.R. Cabrero-Antonino, V. Mainar-Ruiz, M. López-Haro, J.C. Hernández-Garrido, J.J. Calvino, A. Leyva-Pérez, A. Corma, Synthesis of Supported Planar Iron Oxide Nanoparticles and Their Chemo- and Stereoselectivity for Hydrogenation of Alkynes, ACS Catal. 7 (5) (2017) 3721–3729, https://doi.org/10.1021/acscatal.7b0003710.1021/acscatal.7b00037.s001.
[84] D.G. Churchill, K.E. Janak, J.S. Wittenberg, G. Parkin, Normal and inverse primary kinetic deuterium isotope effects for C-H bond reductive elimination and oxidative addition reactions of molybdenocene and tungstenocene complexes: Evidence for benzene σ-complex intermediates, J. Am. Chem. Soc. 125 (2003) 1403–1420, https://doi.org/10.1021/ja027670k.
[85] R. Lin, D. Albani, E. Fako, S.K. Kaiser, O.V. Safonova, N. López, J. Pérez-Ramírez, Design of Single Gold Atoms on Nitrogen-Doped Carbon for Molecular Recognition in Alkyne Semi-Hydrogenation, Angew. Chem. - Int. Ed. 58 (2) (2019) 504–509, https://doi.org/10.1002/anie.201805820.
[86] P. Liu, Y. Zhao, R. Qin, S. Mo, G. Chen, L. Gu, D.M. Chevrier, P. Zhang, Q. Guo, D. Zang, B. Wu, G. Fu, N. Zheng, Photochemical route for synthesizing atomically dispersed palladium catalysts, Science 352 (6287) (2016) 797–800.
[87] J. Yu, J.B. Spencer, First Evidence That the Mechanism of Catalytic Hydrogenation with Homogeneous Palladium and Rhodium Catalysts Is Strongly Influenced by Substrate Polarity, J. Am. Chem. Soc. 119 (22) (1997) 5257–5258, https://doi.org/10.1021/ja964179i.
[88] J. Yu, P.-S. Whitney, J.B. Spencer, Direct comparison between the mechanism of hydrometalation and β- elimination in heterogeneous and homogeneous hydrogenation, J. Mol. Catal. A Chem. 146 (1-2) (1999) 199–210, https://doi.org/10.1016/S1381-1169(99)00102-8.
[89] M.-A. Ha, J. Dadras, A.N. Alexandrova, Rutile-Deposited Pt−Pd clusters: A Hypothesis Regarding the Stability at 50/50 Ratio, ACS Catal. 4 (2014) 3570–3580, https://doi.org/10.1021/cs5011426.
[90] J. Zhang, A.N. Alexandrova, Double σ-Aromaticity in a Surface-Deposited Cluster: Pd4 on TiO2 (110), J. Phys. Chem. Lett. 3 (2012) 751–754, https://doi.org/10.1021/jz300158s.
[91] H. Zhai, A.N. Alexandrova, Local Fluxionality of Surface-Deposited Cluster Catalysts: The Case of Pt_7 on Al_2O_3, J. Phys. Chem. Lett. 9 (7) (2018) 1696–1702, https://doi.org/10.1021/acs.jpclett.8b0037910.1021/acs.jpclett.8b00379.s001.
[92] B. Zandkarimi, A.N. Alexandrova, Dynamics of Subnanometer Pt Clusters Can Break the Scaling Relationships in Catalysis, J. Phys. Chem. Lett. 10 (3) (2019) 460–467, https://doi.org/10.1021/acs.jpclett.8b0368010.1021/acs.jpclett.8b03680.s001.
[93] P.E. Howse, O.T. Jones, I.D.R. Stevens, Synthesis of pheromones, in: Insect Pheromones Their Use Pest Manag., 1998: pp. 226–245. https://doi.org/10.1007/978-94-011-5344-7_7.
[94] T. Ando, S. Inomata, M. Yamamoto, Lepidopteran Sex Pheromones, Top. Current Chem. 239 (2004) 51–96, https://doi.org/10.1007/b95449.
[95] D. Faust Akl, A. Ruiz-Ferrando, E. Fako, R. Hauert, O. Safonova, S. Mitchell, N. López, J. Pérez-Ramírez, Precursor Nuclearity and Ligand Effects in Atomically-Dispersed Heterogeneous Iron Catalysts for Alkyne Semi-Hydrogenation, ChemCatChem. 13 (14) (2021) 3247–3256, https://doi.org/10.1002/cctc.202100235.